coatings

MDPI

Article

Effect of ZrH_2 Doping on Electron Emission Performance of Rare Earth Tungsten Electrode

Shaoxin Zhou, Yingchao Zhang, Shangshang Liang, Jiancan Yang * and Zuoren Nie

Key Laboratory of Advanced Functional Materials, Faculty of Materials and Manufacturing, Ministry of Education of China, Beijing University of Technology, Beijing 100124, China
* Correspondence: yjcan@bjut.edu.cn

Abstract: In order to explore the effect of ZrH_2 on the electron emission performance of rare earth tungsten electrodes (W-La-Y), different proportions of ZrH_2 were added to rare earth tungsten in this study, and samples of three proportions were obtained by ball milling and vacuum hot-pressing sintering. The electron emission performance, phase evolution and surface valence state of the samples were analyzed, respectively. The test results of electrode emission performance show that increasing the mass fraction of ZrH_2 in the range of 0% to 0.1% can continuously improve the electrode emission performance. At 1600 °C, 0.1% ZrH_2 can increase the zero-field current emission density from 0.36 to 0.90 A/cm^2. X-ray diffraction (XRD), the comprehensive thermalgravimetric and differential thermal analysis (TG-DTA) and X-ray photoelectron spectroscopy (XPS) results showed that the ZH_2 added to rare earth tungsten electrodes would react with impurity oxygen in the electrode and consume impurity oxygen, thus reducing the inhibitory effect of impurity oxygen on the electron emission of the electrode and improving its electron emission performance.

Keywords: tungsten electrode; ZrH_2 doped; XPS analysis; electron emission performance

Citation: Zhou, S.; Zhang, Y.; Liang, S.; Yang, J.; Nie, Z. Effect of ZrH_2 Doping on Electron Emission Performance of Rare Earth Tungsten Electrode. *Coatings* **2023**, *13*, 666. https://doi.org/10.3390/coatings13040666

Academic Editor: Barbara Vercelli

Received: 26 February 2023
Revised: 12 March 2023
Accepted: 15 March 2023
Published: 23 March 2023

1. Introduction

In order to develop the application of electrode material to welding, thermal spray, plasma technology and gas discharge light source, many researchers have studied various electrode materials [1–4]. Tungsten has been used to make electrodes due to its high melting temperature and strong thermal electron emission capability. However, the equiaxed crystal that is generated at high temperatures will make the electrodes brittle and decrease electron emission efficiency [1,5]. Langmuir [6] suggested that doping 1%–2% ThO_2 into pure tungsten could improve and stabilize the electron emission capability, as well as improving the efficiency of electron emission. However, due to the radioactivity of thorium, radioactive contamination was inevitable during its production and use, which is harmful to the human body and environment [7,8]. To overcome the shortcomings of ThO_2, rare earth oxides, such as La_2O_3, Ce_2O_3 and Y_2O_3, which are harmless to the human body and environment and have good electron emission performance, have received a lot of attention in the research field of tungsten electrodes [9–14].

Electron emission performance is the most direct factor reflecting the quality of electrode performance. There are numerous factors that affect the electron emission performance, such as density, grain size and oxygen content. Firstly, improving the density of the electrode can, to a certain extent, enhance the electron emission performance and the anti-burnout performance of the electrode. Secondly, reducing the grain size can promote the improvement of the electron emission performance. Chen et al. [15] and others sintered a W-Re cathode and studied the microstructure and electron emission performance of the cathode, and they found that the addition of Re made the grain size smaller, thereby improving the electron emission performance. The oxygen content also affects the electron emission performance of the electrode. A moderate amount of oxygen on the working

surface of the electrode can reduce the work function and promote electron emission to a certain extent. However, if too much impure oxygen is introduced during the electrode preparation process, such as during ball milling and the sintering of the mixed powders, it will cause the tungsten to react with oxygen at high temperatures, resulting in tungsten volatilization and burnout, thereby reducing the service life of the electrode [16,17]. A series of measurements suggested the welding performance of these types of electrodes was better than the tungsten electrode doped with ThO_2, but the measurement condition was limited in using a lower current because the higher current caused serious burning of the tungsten electrodes [18,19].

To alleviate the burning problem, binary composite rare earth tungsten electrodes and ternary composite rare earth tungsten electrodes were developed, whose welding properties were also better than unary composite rare earth tungsten electrodes. Among the research about binary and ternary composite rare earth tungsten electrodes, lots of them are focused on the type of oxide additives and the preparation processes, while are focused on the oxygen content control [8,9,20,21]. This study adds zirconium hydride (ZrH_2) to binary composite rare earth tungsten to control the oxygen content in the electrode, then discusses the electron emission performance and emission mechanism of the electrode added with ZrH_2. This study also aims to provide the theoretical basis for the optimization of the property of tungsten electrodes in practical applications. Thermionic emission materials, in addition to their applications in the fields of electron sources and vacuum tubes, are also potential candidates for use in energy-related applications, such as thermoelectric generators and solar cells, as well as for use as electrode materials in electron thermionic cooling (ETC). Therefore, there is an urgent need for electrode materials with lower work functions and better anti-burnout properties.

2. Experimental

2.1. Sample Preparation

A mixture consisting of W, La_2O_3, Y_2O_3 and ZrH_2 was prepared. While keeping the mass fraction of the La_2O_3 powder (500 nm, 99.9%, Xuzhou Boguan Welding Material Co., Ltd., Xuzhou, China) and Y_2O_3 powder (500 nm, 99.9%, Xuzhou Boguan Welding Material Co., Ltd., Xuzhou, China) consistent, the mass fractions of the W powder (2 μm, 99.99%, Xiamen Tungsten Co., Ltd., Xiamen, China) and ZrH_2 powder (10 μm, 99.5%, Changsha Tianjiu Metal Materials Co., Ltd., Changsha, China) were changed to prepare three mixtures, as shown in the Table 1. After the powder was fully mixed, it would be put into a ball mill jar using a planetary ball mill (QM-3SP2, Nanjing Nanda Instrument Plant, Nanjing, China) for mechanical mixing and then sintered by a vacuum hot pressing sintering furnace (ZT-40-21Y, Shanghai Chenhua Electric Furnace Co., Ltd., Shanghai, China) to obtain rare earth tungsten electrodes. The ratio of ball to the material during ball milling was 8:1, the speed of the ball mill was 400 r/min, the ball milling time was 10 h and every 2.5 h it was stopped for 15 min. The parameters of vacuum hot-pressing sintering are listed as follows: the sintering temperature was 1600 °C, the sintering pressure was 60 MPa, the holding time was 60 min, the heating rate was 10 °C/min at the range of 0–1000 °C while 4 °C/min at the range of 1000–1600 °C and the vacuum degree in the sintering process was 10^{-3} Pa. Finally, a sintered block of Φ 20 mm × 8 mm was obtained. The specific composition of the material is shown in Table 1.

Table 1. The composition of the material.

Sample	W	La_2O_3 (wt.%)	Y_2O_3 (wt.%)	ZrH_2 (wt.%)
1#	Bal.	1.5	0.08	0
2#	Bal.	1.5	0.08	0.05
3#	Bal.	1.5	0.08	0.1

2.2. Material Analysis and Testing

The phase analysis of the electrode was carried out using X-ray diffraction (XRD, XRD-7000, Shimadzu, Kyoto, Japan). The comprehensive thermal-gravimetric and differential thermal analysis (TG-DTA, Labsys Evo, Setaram instrumentation, Lyon, France) were carried out to study the phase changes. The grain size of the electrode was analyzed by the metallographic microscope. The etching solution used for metallographic sample preparation was NaOH:$K_3Fe(CN)_6$:H_2O=1:1:8. The microstructure and elemental composition were characterized using scanning electron microscopy (SEM, FEI Quanta 650, FEI, Hillsboro, OR, USA) and an energy dispersive spectrometer (EDS).

The surface composition and valence state of the electrodes were analyzed using X-ray photoelectron spectroscopy (XPS, Thermo Fisher ESCALAB 250Xi, FEI, Hillsboro, OR, USA), where the X-ray was Al kα (1486.6 eV) generated from an anode target. During the experiment, the vacuum degree of the analysis chamber was better than 1×10^{-9} mbar, and the vacuum degree of the preparation chamber was better than 1×10^{-7} mbar. The X-ray spot was 500 μm. The through energy of the narrow spectrum of O1s, La3d, Zr3d and W4f were 30 eV. The step size was 0.05 eV, and the duration of each point was 100 ms. The measured data were analyzed using the Casa XPS data analysis software. First, the peak position of the sample was corrected with contamination carbon (284.8 eV), and the background was deducted by the Shirley method. When performing split-peak fitting, different fitting methods were used according to the different spectra. Gaussian–Lorentzian GL was used to fit the symmetrical peaks of the non-metallic, and LF was used to fit the asymmetrical peaks of the pure metal. In addition, quantitative analysis was performed according to the strength of each characteristic peak in the XPS spectrum, the sensitivity factor method was used for the analysis and the sensitivity factor was researched according to the database of the software.

The electron emission performance of the electrodes was tested on the electron emission performance test bench with an ion pump and a molecular pump system. This test adopts a short-range flat diode structure. The cathode is heated by a tantalum foil with a thickness of 0.05 mm, the cathode surface and the bottom surface of the cathode shield are on the same plane, the distance between the cathode and anode is 0.5 mm and the cathode temperature is measured by an infrared thermometer. The ultimate background pressure of the vacuum system is lower than 1×10^{-7}. The cathode is slowly heated and the vacuum degree is in the order of 5×10^{-6} Pa during the experiment. The obtained I–U curves were processed using the software Cathode601-723.

3. Results and Discussion

3.1. Emission Performance of the Electrode Material

Figure 1a–c shows the volt–ampere characteristic curves of electrodes doped with different fractions of ZrH_2. It can be seen that the emission current of the material increases with the increase of the voltage, and the current changes greatly when the voltage is low. When the $\sqrt{U}$ is higher than 10, the currents change slowly and become stable gradually. Figure 1d shows the zero-field emission current density of the electrode materials with 0% ZrH_2, 0.05% ZrH_2 and 0.1% ZrH_2 at different temperatures, which is obtained using the Schottky epitaxy method. It is found that the zero-field emission current density of the material increases with the increase of temperature. In detail, the change of the zero-field emission current density is subtle when the temperature is lower than 1450 °C and increases significantly after the temperature is higher than 1500 °C. The zero-field emission current density of 0% ZrH_2 electrode is 0.01 and 0.36 A/cm^2 at 1450 and 1600 °C, respectively. For the 0.05% ZrH_2 electrode, it can reach 0.03 A/cm^2 at 1450 °C and as high as 0.87 A/cm^2 at 1600 °C, which indicates that adding ZrH_2 could reduce the temperature by at least 50 °C to acquire the same zero-field emission current density, compared with the electrodes without ZrH_2. The zero-field emission current density at 1600 °C is 0.36, 0.87, and 0.90 A/cm^2, respectively, indicating that the zero-field emission current density and

the electron emission capability of the electrode gradually increases after adding zirconium hydride gradually.

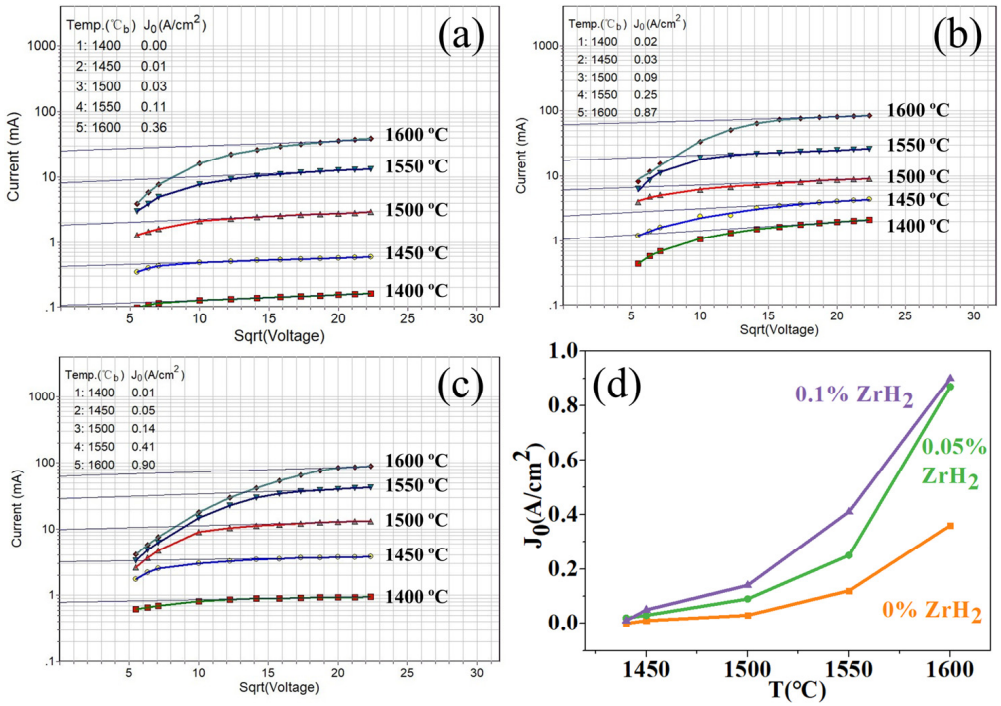

Figure 1. Volt–ampere characteristic curves (**a**) 0% ZrH_2; (**b**) 0.05% ZrH_2 and (**c**) 0.1% ZrH_2; (**d**) zero-field emission current density of the electrode materials.

3.2. Analysis of XRD and TG-DTA

Figure 2 is the XRD pattern of the bulk electrode material prepared by vacuum hot-pressing sintering. In addition to W and La_2O_3, a new phase $La_2Zr_2O_7$ (PDF#17-0450, LZO) appears in the electrode after sintering. When the ZrH_2 content was 0%, the LZO phase was not observed, but when the ZrH_2 content increased to 0.05% and 0.1%, the LZO phase was observed. With the increase of the amount of doping ZrH_2, the diffraction peak intensity of LZO also increases.

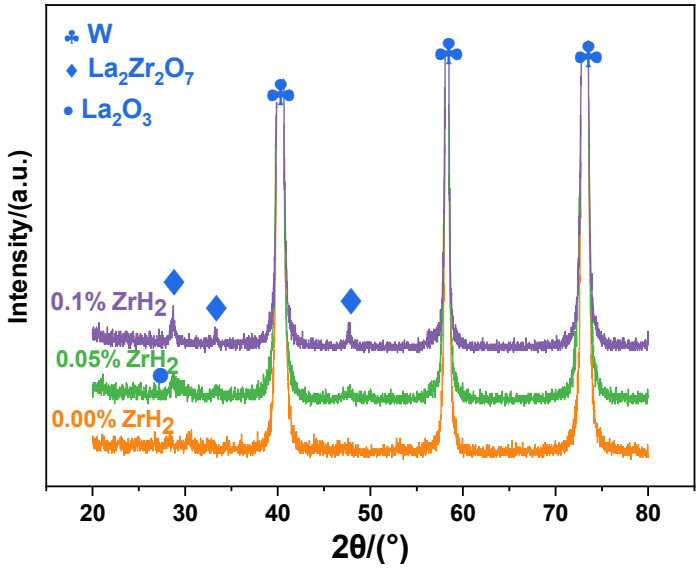

Figure 2. XRD pattern of different samples.

In order to study the reasons for its phase change, the TG-DTA of the mixed powder was carried out in an argon atmosphere, and the results are shown in Figure 3. It can be seen from Figure 3 that in the range of 0–298 °C at the TG curve, the weight lost was 0.3%, while the corresponding DSC curve showed an obvious endothermic peak, which was mainly due to the loss of the water absorbed in the intergranular and other substances. At 400 °C, an obvious exothermic peak appears in the DTA curve, which means a small part of the metal tungsten undergoes oxidation reaction to form tungsten oxide. At 512–700 °C, there are three obvious endothermic peaks on the DTA curve, among which the endothermic peaks at 512 and 587 °C are small and wide, while the endothermic peak at approximately 656 °C is sharp and obvious, indicating that ZrH_2 begin to decompose into hydrogen and active zirconium at 512 °C, and the decomposition is completed at approximately 656 °C. This process is consistent with the literature [22], which reported that the decomposition temperature of ZrH_2 is in the range of 500 to 700 °C. In the range from 740 to 1000 °C, active zirconium combines with oxygen to form zirconium–oxygen compounds. Meanwhile, tungsten oxide is reduced to metal tungsten under the action of hydrogen. Finally, when the temperature is above 1000 °C, the zirconium oxide compound combines with part of La_2O_3 in the electrode to form $La_2Zr_2O_7$ [23]. During the sintering process, ZrH_2 is dehydrogenated in the range of 500–700 °C, and the generated active element Zr will absorb the oxygen in the rare earth tungsten electrode (especially the oxygen at the grain boundary) to form a zirconium oxide compound. Finally, the zirconium oxide compound combines with part of La_2O_3 to form LZO. Therefore, as the doping amount of ZrH_2 increases, the electron emission capability of the electrode is gradually enhanced due to the release of hydrogen from ZrH_2 at 500 to 700 °C, and the generated active zirconium will absorb the impurity oxygen at the tungsten grain boundary. With the increase of ZrH_2 content, more impurity oxygen content is absorbed and the negative effect of excess oxygen on electron emission is reduced, so the electron emission capability of the electrode is enhanced.

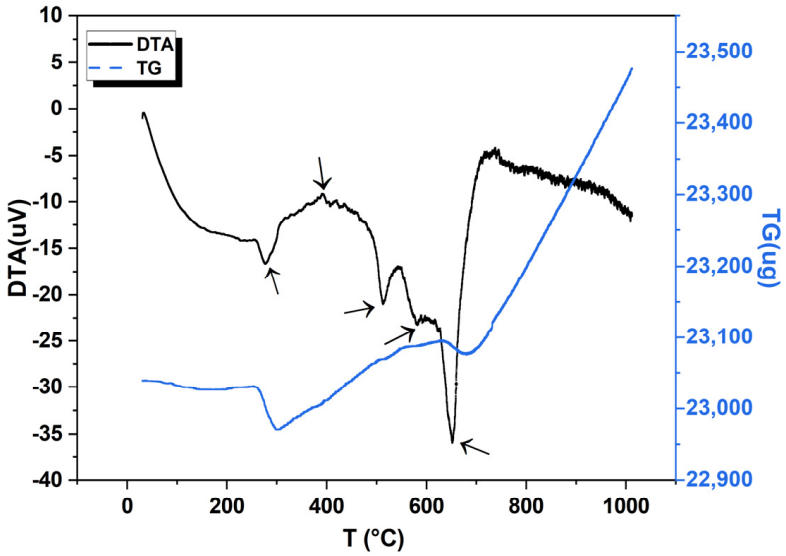

Figure 3. TG−DTA curve of the mixed powder sample.

3.3. SEM and Metallographic Analysis

In order to observe the surface morphology of the electrode doped with ZrH_2, SEM and EDS analyses were conducted. Figure 4 shows the SEM and EDS images of the sample without doping ZrH_2. The sample has two distinct contrasts, including dark and light. EDS analysis of the light area (point 2) shows that this area is metal W, and EDS analysis of the dark area (point 1) shows that this area is rare earth oxide La_2O_3. Figure 5 shows the SEM and EDS images of the sample doping with 0.05% ZrH_2. EDS analysis of the dark particle point 1 shows that the main elements are La, Zr and O. It can be speculated that

the substance at point 1 is a newly generated phase LZO. The energy spectrum analysis of point 2 shows that the main elements are La and O, and it is speculated that the particles at point 2 are rare earth oxide La_2O_3.

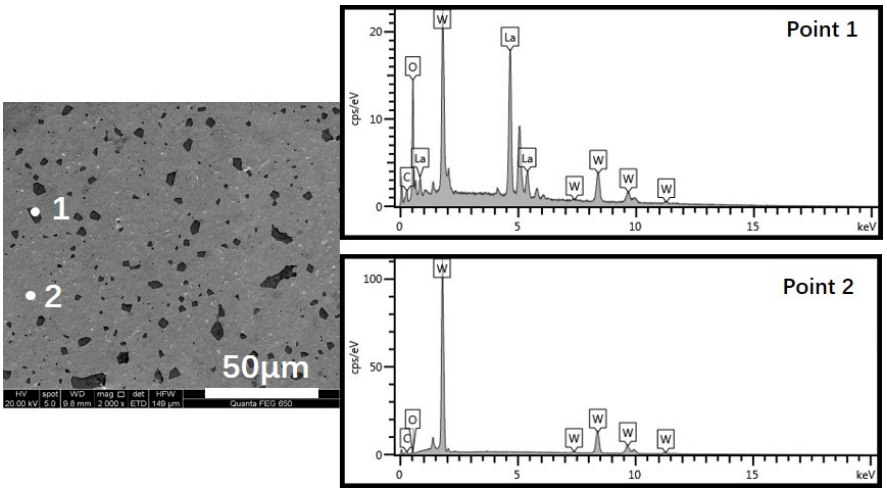

Figure 4. SEM and EDS images of the sample without doping ZrH_2.

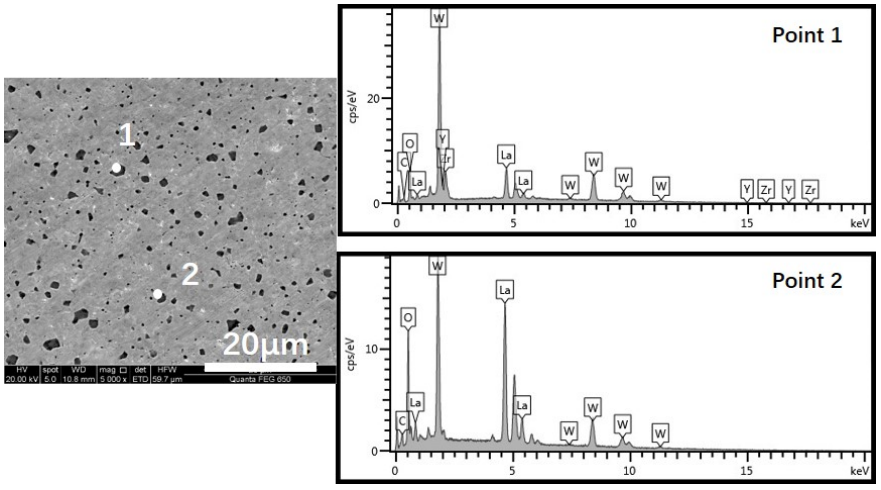

Figure 5. SEM and EDS images of the sample doped with 0.05% ZrH_2.

Figure 6 shows the SEM and EDS images of the sample doping with 0.1% ZrH_2. Similar to 0.05% ZrH_2, 0.1% ZrH_2 led to the generation of new phase LZO and rare earth oxide La_2O_3. In summary, in the electrode material without zirconium hydride, the rare earth oxide La_2O_3 is dispersed in the tungsten matrix in a circular or irregular shape. After adding zirconium hydride, the decomposition of the zirconium generated hydrogen and active zirconium, which has a strong affinity with oxygen. Thus, the impurity oxygen at the tungsten grain boundary will be absorbed or the oxygen in rare earth oxides will be captured, resulting in the formation of zirconium dioxide. Zirconia will diffuse to the grain boundaries of La_2O_3 and react with part of La_2O_3 in the sample to form LZO. Because the content of the generated ZrO_2 is much lower than that of La_2O_3, the majority of La_2O_3 remains in the sample in its original form. Therefore, the topography in Figure 6 shows that La_2O_3 and the generated new phase LZO are dispersed in the tungsten matrix.

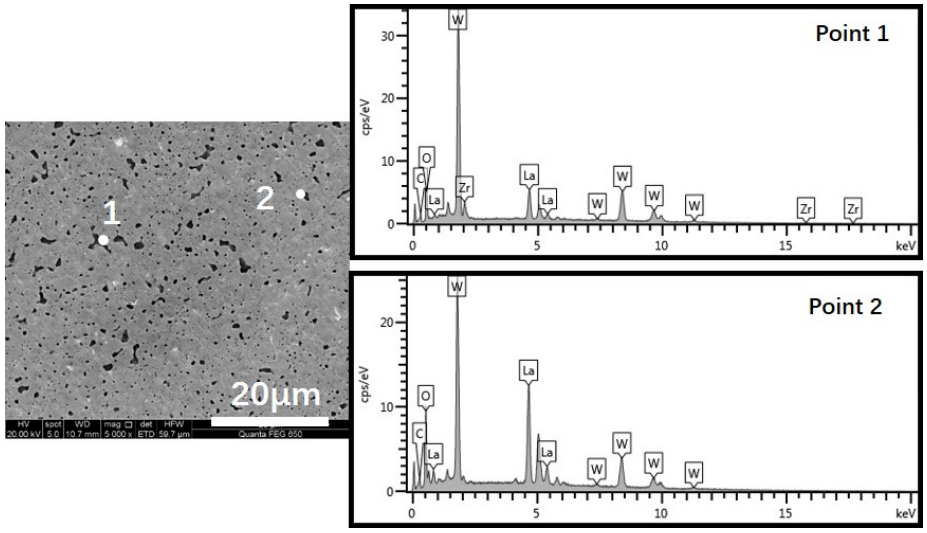

Figure 6. SEM and EDS images of the sample doped with 0.1%ZrH_2.

The particle size analysis of the second phase in the SEM image shows that with the increase of ZrH_2 content, the average size of the second phase decreases gradually. When the size of the second phase is reduced to the nanometer level, it is beneficial to improve the electron emission performance of rare earth tungsten. The contact between the tungsten matrix and the second-phase particles forms the circuit between the metal and the semiconductor. According to the principle of field emission, the existence of the electric field will reduce the height and width of the potential barrier on the cathode surface. When the width of the potential barrier is reduced to less than the mean freedom of electrons, the electrons will have a tunneling effect, cross the potential barrier on the surface of the cathode and escape into the vacuum [24]. When the size of the second-phase particles in the electrode is reduced to the nanometer level, the tunneling effect is more likely to occur, that is, the second-phase particles are more likely to cross the potential barrier on the electrode surface and be emitted into the vacuum. Therefore, with the increase of the content of zirconium hydride, the electron emission performance is gradually improved.

Figure 7 is the metallographic diagram and grain size diagram of the electrodes doped with 0% ZrH_2, 0.05% ZrH_2 and 0.1% ZrH_2. Grains within the selected field of view are statistically analyzed using the intercept method [25]. It can be seen from the figure that the LZO particles and the remaining La_2O_3 are distributed at the grain boundaries, and the grain size of the electrode has changed significantly after doping with ZrH_2. The average W grain sizes of the electrodes doped with 0% ZrH_2, 0.05% ZrH_2 and 0.1% ZrH_2 are approximately 10.75, 7.4 and 5.56 μm, respectively. Thus, it can be concluded that the doping of ZrH_2 can significantly reduce the average grain size of rare earth tungsten electrodes.

The doping of ZrH_2 can effectively inhibit the growth of tungsten grains since the doping of ZrH_2 generates a new phase LZO which is mainly dispersed in the tungsten grain boundary. By pinning the grain boundaries, the movement of grain boundaries and dislocations as well as the diffusion of substances are prevented, thereby preventing the connection and aggregation between W grains. In the initial stage of vacuum hot-pressing sintering, some W grains that have small angles will rotate and merge and grow into coarse W grains. However, the doping of ZrH_2 will form La-Zr-O grains, blocking the contact between W grains and avoiding the aggregation of W grains under high temperatures, so it can prevent the merging and growing behavior of W grains. In addition, the reduction of the grain size is beneficial to the increase of the activation energy and contact area between the cathode surface active layer and the base metal, thereby forming the new active layer, which promotes electron emission from the electrode. Thus, the gradual reduction of the tungsten grain size is beneficial to the improvement of the electron emission performance.

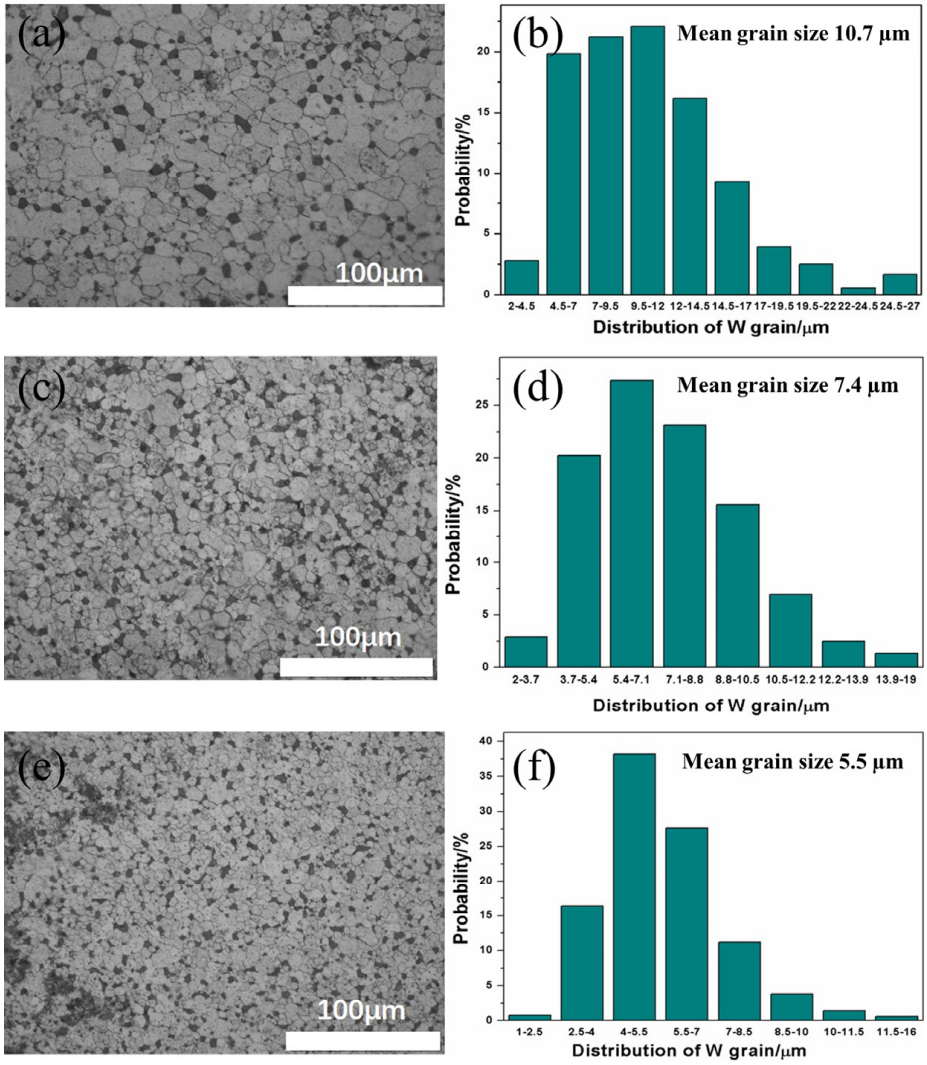

Figure 7. Metallographic diagram and grain size map of the samples doped with ZrH_2 (**a**,**b**) 0%; (**c**,**d**) 0.05% and (**e**,**f**) 0.1%.

3.4. XPS Analysis

Because the tungsten electrode discharge occurs only on the sample surface, it is necessary to perform composition and valence analysis on the sample surface. Figure 8 shows the full XPS spectrum of the unheated 0.1% ZrH_2 rare earth tungsten electrode. It can be seen from the figure that the main elements on the surface of the sintered sample are W, La, O and C. Among W is the matrix. Part of La is from the added rare earth oxide La_2O_3, and part of it is from La_2O_3-ZrO_2 and LZO. Part of O is the lattice oxygen in the sample, and the other part is the adsorbed oxygen of the sample. C is the adsorbed carbon on the surface of the sample. C is used to calibrate the peak position of the sample. No Zr element was detected in the full spectrum because the addition of zirconium hydride was only 0.1%, and the detection depth of XPS was approximately 10 nm. There may be no Zr in the analysis area, so there is no obvious Zr characteristic peak in the spectrum. The quantitative analysis of each element in the full spectrum is shown in Table 2.

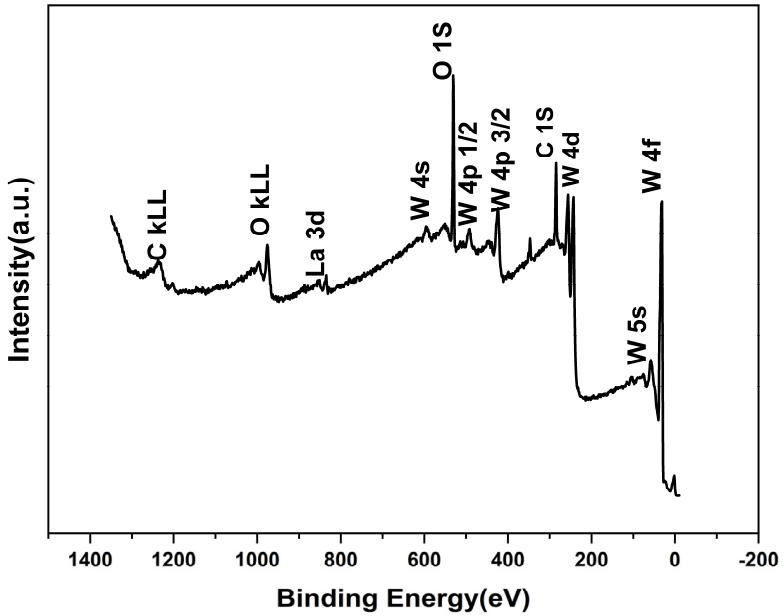

Figure 8. XPS survey of unheated 0.1% ZrH_2.

Table 2. Relative content of unheated 0.1% ZrH_2 surface.

Unit	W	La	O	Zr
At. %	43.98	0.54	55.48	0.00

Figure 9 is the XPS spectrum of the unheated sample O1s. Figure 9a is an O1s diagram of the component that was added with 0% ZrH_2, and the oxygen-related components in this component are mainly La_2O_3. It can be found that the O1s peak is fitted by three peaks of O1, O2 and O3. The binding energies of O1, O2 and O3 are 530.24, 530.98 and 532.22 eV, respectively. O1 (530.24 eV) is considered to be part of the oxygen in La_2O_3 [26–29]. La_2O_3 has a hexagonal structure [30], all La atoms are distributed in the same position and the coordination number with O is 7. The oxygen atoms are distributed in two different positions. Two-thirds of the oxygen atoms are 4-coordinated, attributed to O1, whose La-O bond length is 2.36 Å. The remaining third of the oxygen atoms are 6-coordinated, attributed to O2, and the La-O bond has a length of 2.72 Å [31]. O1 and O2 have chemical shifts due to the coordination number and bond length difference. Reference [32] calculated the bond valences of O1 and O2 in La_2O_3, and the results show that the negative charge in O1 is higher than that of O2, which indicates that O1 is located at the low binding energy end and O2 is at the high binding energy end in the XPS spectrum. In XPS, when the core electrons are excited, the electrons in the inner layer are in the excited state and the electrons in other orbitals will be adjusted, that is, the electron relaxation process occurs, which will cause the electron orbits to shrink or expand. After the process, the ion returns to the ground state and releases relaxation energy. The difference between the coordination number and the bond length will lead to the difference in the extra-atomic relaxation energy [33]. In order to determine the correctness of the relative positions of the above binding energies of O1 and O2, relaxation energy R^{ea} was calculated using Formula (1) [34].

$$R^{ea} = \frac{7.2n\alpha}{R^4 + RD\alpha} \quad (1)$$

where n represents the coordination number; α represents the electron polarizability of the ligand (La is 1.05 $Å^3$); R is bond length; D is the geometric factor and takes 2.37 [35]. Through Formula (1), the extra-atomic relaxation energy Rea of O1 is calculated to be 0.82 eV, and the extra-atomic relaxation energy Rea of O2 is 0.73 eV. Since the relaxation pro-

cess occurs almost simultaneously with the photoelectron emission process, the relaxation process will accelerate the photoelectrons, increase the kinetic energy of the photoelectrons and reduce the binding energy. Therefore, the binding energy of O1 is lower than that of O2, which verifies the correctness of the relative positions of the two binding energies. In addition, O3 is in the high binding energy position to other impurities, such as adsorbed oxygen [27,28], and it is the surface oxygen atom, such as OH^- or O^{1-} [35].

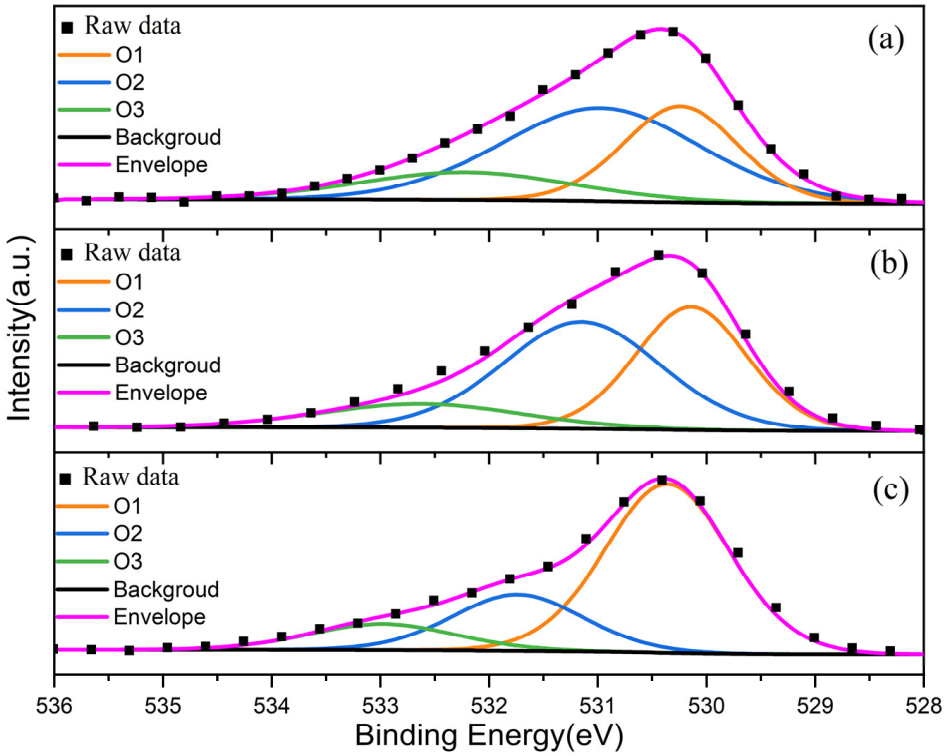

Figure 9. O1s of XPS spectrum for samples (**a**) 0% ZrH_2, (**b**) 0.05% ZrH_2 and (**c**) 0.1% ZrH_2.

Figure 9b,c are the O1s spectra with 0.05% ZrH_2 and 0.1% ZrH_2 added, respectively, which show that the binding energy positions of O1 and O2 have changed significantly. For the sample with 0.05% ZrH_2, the binding energies of O1 and O2 are 530.14 and 531.15 eV, respectively. Compared with the sample with 0% ZrH_2, the peak of O1 has a negative chemical shift of 0.1 eV, and the peak of O2 has a positive chemical shift of 0.17 eV. When the addition amount of ZrH_2 is 0.1%, the peak positions of O1 (530.43 eV) and O2 (531.81 eV) shift to the higher binding energy position. Compared with the sample with 0% ZrH_2, the peaks of O1 and O2 have a positive chemical shift of 0.19 and 0.83 eV, respectively. This apparent chemical shift means that the O atom may be bonded to some elements with stronger electronegativity than La [36,37]. The electronegativity of La in the La-O bond is 1.1, while that of Zr is 1.33, so it suggests that a part of La-O bonding becomes La-Zr-O bonding after adding zirconium hydride. Moreover, it can be inferred in Figure 9a–c that O3 has the high binding energy of all impurity oxygen, and O1 and O2 are the sums of lattice oxygen. The calculated contents of impurity oxygen and total lattice oxygen in the samples with 0% ZrH_2, 0.05% ZrH_2 and 0.1% ZrH_2 are shown in Figure 10. Therefore, with the increase of zirconium hydride content, the content of impurity oxygen gradually decreases and the content of lattice oxygen gradually increases, indicating that the active zirconium generated by the decomposition of zirconium hydride absorbs the impurity oxygen in the sample and effectively reduces the amount of oxygen in the sample. The content of lattice oxygen is relatively increased due to the formation of ZrO_2. Therefore, the emission performance of the tungsten electrode is improved.

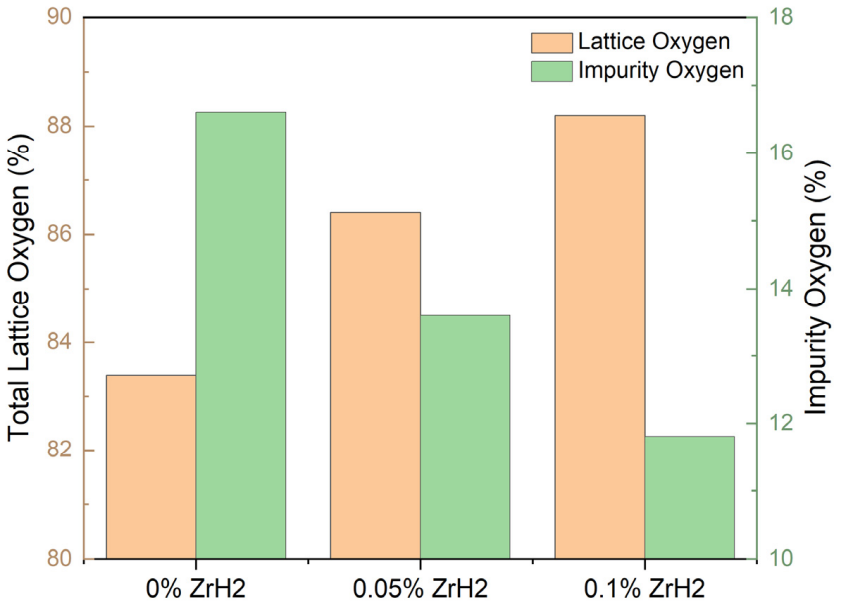

Figure 10. The content of impurity oxygen and total lattice oxygen.

Though the experimental study has suggested the merits of ZrH_2 doping for the electron emission performance of rare earth tungsten electrode, two limitations should also be considered for practical usage. The first one is that doping ZrH_2 into tungsten alloy can affect the material's ability to be machined. The second is that ZrH_2 is relatively expensive and doping it into tungsten alloy electrodes can increase the cost of the electrodes. This can be a limiting factor for applications where cost is an important consideration.

4. Conclusions

In this work, the different proportions of ZrH_2 were added to rare earth tungsten to explore the effect of ZrH_2 on the electron emission performance of rare earth tungsten electrodes. The electron emission performance, phase evolution and surface valence state of the samples were analyzed. The following conclusions can be drawn:

(1) Adding ZrH_2 to rare earth tungsten electrodes will consume the impurity oxygen in the electrode and generate $La_2Zr_2O_7$ particles.
(2) With the addition of ZrH_2, the size of tungsten grains and the size of second-phase particles will gradually become smaller, which will promote the uniform distribution of the activated substance.
(3) With the addition of ZrH_2, the content of impurity oxygen is gradually decreasing and the content of lattice oxygen is gradually increasing. The decrease of the impurity oxygen content will improve the electron emission performance of the electrode.

Author Contributions: Conceptualization, J.Y.; Methodology, S.Z., Y.Z., S.L. and J.Y.; Formal analysis, Y.Z.; Writing—original draft, S.Z.; Funding acquisition, Z.N. All authors have read and agreed to the published version of the manuscript.

Funding: This work was supported by the National Key R&D Program of China (2021YFB3501102).

Institutional Review Board Statement: Not applicable.

Informed Consent Statement: Not applicable.

Data Availability Statement: Not applicable.

Conflicts of Interest: The authors declare no conflict of interest.

References

1. Zhou, M.L.; Zhang, J.X.; Nie, Z.R.; Wang, J.S.; Zuo, T.Y. Study on thermionic properties of tungsten and molybdenum doped with rare earth oxides and their application. *China Tungsten Ind.* **2001**, *16*, 52–56.
2. Nakata, D.; Toki, K.; Funaki, I.; Kuninaka, H. Performance of ThO_2-W, Y_2O_3-W and La_2O_3-W cathodes in quasi-steady magneto-plasmadynamic thrusters. *J. Propul. Power* **2011**, *27*, 912–915. [CrossRef]
3. Zhang, Y.C.; Wang, P.; Yang, J.C.; Zhou, S.X.; Zhang, P.; Nie, Z.R. Study on morphology and chemical states of surface active layer of Ce-W cathode. *Appl. Surf. Sci.* **2019**, *479*, 815–821. [CrossRef]
4. Wang, K.; Liu, W.; Hong, Y.; Sohan, H.M.S.; Tong, Y.; Hu, Y.; Zhang, M.; Zhang, J.; Xiang, D.; Fu, H.; et al. An overview of technological parameter optimization in the case of laser cladding. *Coatings* **2023**, *13*, 496. [CrossRef]
5. Zhou, M.L.; Nie, Z.R.; Chen, Y.; Zhang, J.X.; Zuo, T.Y. Research and development of Re-tungsten electrodes. *China Tungsten Ind.* **2000**, *15*, 30–34.
6. Langmuir, I. The electron emission from thoriated tungsten filaments. *Phys. Rev.* **1923**, *22*, 357–398. [CrossRef]
7. Paschen, P. Alternatives to thorium additions to tungsten-based materials. *JOM* **1996**, *48*, 45–47. [CrossRef]
8. Yang, J.C.; Nie, Z.R.; Zhou, M.L.; Xi, X.L. On tungsten electrode doped with rare earth oxides. *China Tungsten Ind.* **2007**, *22*, 39–44.
9. Cui, Y.T.; Zhang, S.G.; Wang, M.; Zhang, X.; Ren, X.J. Study on rare earths doped tungsten cathode for high performance plasma spray torch. *Therm. Spray Technol.* **2014**, *6*, 24–27.
10. Yang, J.C.; Cao, J.; Zhang, X.; Huang, L. Welding performance of several rare earth tungsten electrodes in 5A62 aluminum alloy. *J. Beijing Univ. Technol.* **2014**, *40*, 1561–1564.
11. Zhang, X.X.; Yan, Q.Z. Morphology evolution of La_2O_3 and crack characteristic in W-La_2O_3 alloy under transient heat loading. *J. Nucl. Mater.* **2014**, *451*, 283–291. [CrossRef]
12. Hoebing, T.; Hermanns, P.; Bergner, A.; Ruhrmann, C.; Traxler, H.; Wesemann, I.; Knabl, W.; Mentel, J.; Awakowicz, P. Investigation of the flickering of La_2O_3 and ThO_2 doped tungsten cathodes. *J. Appl. Phys.* **2015**, *118*, 023306. [CrossRef]
13. Li, J.F.; Cheng, J.G.; Wei, B.Z.; Zhang, M.L.; Luo, L.M.; Wu, Y.C. Microstructure and properties of La_2O_3 doped W composites prepared by a wet chemical process. *Int. J. Refract. Met. Hard Mater.* **2017**, *66*, 226–233. [CrossRef]
14. Cui, Y.T.; Li, B.S.; Peng, Y.; Wang, L.Y.; Yang, J.C. Study on welding performance and fabrication of tungsten electrode doped with non-radiating rare earths oxide. *Therm. Spray Technol.* **2013**, *5*, 65–68.
15. Lai, C.; Wang, J.; Zhou, F.; Liu, W.; Engelsen, D.; Miao, N. Emission and evaporation properties of 75 at.% Re-25 at.% W mixed matrix impregnated cathode. *Appl. Surf. Sci.* **2018**, *427*, 874–882. [CrossRef]
16. Xie, Z.M.; Liu, R.; Zhang, T.; Fang, Q.F.; Liu, C.S.; Liu, X.; Luo, G.N. Achieving high strength/ductility in bulk W-Zr-Y_2O_3 alloy plate with hybrid microstructure. *Mater. Des.* **2016**, *107*, 144. [CrossRef]
17. Ren, C.; Fang, Z.Z.; Koopman, M.; Butler, B.; Paramore, J.; Middlemas, S. Methods for improving ductility of tungsten-a review. *Int. J. Refract. Met. Hard Mater.* **2018**, *75*, 170–183. [CrossRef]
18. Lassner, E.; Schubert, W.D. *Tungsten Properties, Chemistry, Technology of the Element, Alloys, and Chemical Compounds*; Plenum Publishers: New York, NY, USA, 1999.
19. Sadek, A.A.; Ushio, M.; Matsuda, F. Effect of rare earth metal oxide additions to tungsten electrodes. *Metall. Trans. A* **1990**, *21*, 3221–3236. [CrossRef]
20. Huang, L.; Jiang, L.; Topping, T.D.; Dai, C.; Wang, X.; Carpenter, R.; Haines, C.; Schoenung, J.M. In situ oxide dispersion strengthened tungsten alloys with high compressive strength and high strain-to-failure. *Acta Mater.* **2017**, *122*, 19–31. [CrossRef]
21. Xue, J.; Guo, W.; Yang, J.; Xia, M.S.; Zhao, G.; Tan, C.W.; Wan, Z.D.; Chi, J.X.; Zhang, H. In-situ observation of microcrack initiation and damage nucleation modes on the HAZ of laser-welded DP1180 joint. *J. Mater. Sci. Technol.* **2023**, *148*, 138–149. [CrossRef]
22. Zhang, H.; Shen, H.S.; Che, X.K.; Wang, L.J. Zirconium powder production through hydrogenation and dehydrogenation process. *Chin. J. Rare Met.* **2011**, *35*, 417–421.
23. Huang, Z.; Li, S.S.; Tan, C.; Liu, J.H.; Lu, L.L.; Zhang, S.W.; Zhang, H.J. La2Zr_2O_7 powder with pyrochlore structure by molten salt synthesis. *Mate. Mech. Eng.* **2016**, *40*, 55–58. [CrossRef]
24. Wang, X.G.; Song, H.; Wang, M.L.; Ding, B.J. Effects of second phase particle size on electron emission ability of Mo-La_2O_3 Cathode. *Rare Met. Mater. Eng.* **2010**, *11*, 51–55.
25. Hua, S.M. Discussion on the evaluation method of measurement uncertainty of grain size. *Qual. Tech. Superv. Res.* **2015**, *2*, 9–11.
26. NIST X-ray Photoelectron Spectroscopy Database. Version 3.5 ed. National Institute of Standards and Technology Gaithersburg. 2010. Available online: http://srdata.nist.gov/xps/ (accessed on 1 December 2010).
27. Howng, W.Y.; Thorn, R.J. Investigation of the electronic structure of $La_{1-x}(M^{2+}) \times CrO_3$, Cr_2O_3 and La_2O_3 by X-ray photoelectron spectroscopy. *J. Phys. Chem. Solids* **1980**, *41*, 75–81. [CrossRef]
28. Uwamino, Y.; Ishizuka, T.; Yamatera, H. X-ray photoelectron spectroscopy of rare-earth compounds. *J. Electron. Spectrosc. Relat. Phenom.* **1984**, *34*, 67–78. [CrossRef]
29. Kumar, R.; Mintz, M.H.; Rabalais, J.W. Surface recoiling XPS and UPS study of chemisorption of H_2O_2 and H_2O on lanthanum. *Surf. Sci.* **1984**, *147*, 37–47. [CrossRef]
30. Marsella, L.; Fiorentini, V. Structure and stability of rare-earth and transition-metal oxides. *Phys. Rev. B* **2004**, *69*, 172103. [CrossRef]

31. Sunding, M.F.; Hadidi, K.; Diplas, S.; Løvvik, O.M.; Norby, T.E.; Gunnæs, A.E. XPS characterisation of in situ treated lanthanum oxide and hydroxide using tailored charge referencing and peak fitting procedures. *J. Electron. Spectrosc. Relat. Phenom.* **2011**, *184*, 399–409. [CrossRef]
32. Parthé, E. *Modern Perspectives in Inorganic Crystal Chemistry*; Springer Science & Business Media: Berlin/Heidelberg, Germany, 1992; pp. 163–175.
33. Giuliano, M. Auger parameter shifts in the case of the non-local screening mechanism: Applications of the electrostatic model to molecules, solids and adsorbed species. *Surf. Interface Anal.* **1991**, *17*, 352–356.
34. Moretti, G. Auger parameter and wagner plot in the characterization of chemical states by X-ray photoelectron spectroscopy: A review. *J. Electron. Spectrosc. Relat. Phenom.* **1998**, *95*, 95–144. [CrossRef]
35. Stoychev, D.; Valov, I.; Stefanov, P.; Atanasova, G.; Stoycheva, M.; Marinova, Ts. Electrochemical growth of thin La_2O_3 films on oxide and metal surfaces. *Mater. Sci. Eng. C* **2003**, *23*, 123–128. [CrossRef]
36. Jafer, R.M.; Coetsee, E.; Yousif, A.; Keoon, R.E.; Ntwaeaborwa, O.M.; Swart, H.C. X-ray photoelectron spectroscopy and luminescent properties of Y_2O_3:Bi^{3+} phosphor. *Appl. Surf. Sci.* **2015**, *332*, 198–204. [CrossRef]
37. Zhu, J.Q.; Zhu, Y.K.; Shen, W.X.; Wang, Y.J.; Han, J.C.; Gui, T.; Peng, L.; Bing, D. Growth and characterization of yttrium oxide films by reactive magnetron sputtering. *Thin Solid Films* **2011**, *519*, 4894–4898. [CrossRef]